Possible artifacts in dynamic CEST MRI due to motion and field alterations

Moritz Zaiss [a],*, Kai Herz [a], Anagha Deshmane [a], Mina Kim [b], Xavier Golay [b], Tobias Lindig [c], Benjamin Bender [c], Ulrike Ernemann [c], Klaus Scheffler [a,d]

[a] High-field Magnetic Resonance Center, Max Planck Institute for Biological Cybernetics, Tübingen, Germany
[b] Brain Repair & Rehabilitation, Institute of Neurology, University College London, United Kingdom
[c] Department of Diagnostic and Interventional Neuroradiology, Eberhard-Karls University Tübingen, Tübingen, Germany
[d] Department of Biomedical Magnetic Resonance, Eberhard-Karls University Tübingen, Tübingen, Germany

ARTICLE INFO

ABSTRACT

Purpose: Dynamic CEST studies such as dynamic glucose enhanced imaging, have gained a lot of attention recently. The expected CEST effects after injection are rather small in tissue especially at clinical field strengths (0.5–2%). Small movements during the dynamic CEST measurement together with a subtraction-based evaluation can lead to pseudo CEST effects of the same order of magnitude. These artifacts are studied herein.
Methods: A brain tumor patient 3D-CEST baseline scan without glucose injection performed at 3 T is used to generate a virtual dynamic measurement introducing different kinds of simulated motion and B_0 shifts.
Results: Minor motion (0.6 mm translations) and B_0 artifacts (7 Hz shift) can lead to pseudo effects in the order of 1% in dynamic CEST imaging. Especially around tissue interfaces such as CSF borders or tumor affected areas, the pseudo effect patterns are non-intuitive and can be mistaken as dynamic agent uptake.
Conclusion: Correction or mitigation for small motions is crucial for dynamic CEST imaging, especially in subjects with lesions. Concomitant B_0 alterations can as well induce pseudo CEST effects at 3 T.
© 2018 The Authors. Published by Elsevier Inc. This is an open access article under the CC BY license (http://creativecommons.org/licenses/by/4.0/).

1. Introduction

Since it was first demonstrated by Wolff and Balaban in 1990 [1], chemical exchange saturation transfer (CEST) has emerged as an alternative MRI contrast [2–5]. Among numerous key biomolecules which can be indirectly detected via their chemical exchange with water, ᴅ-glucose or its analogues in particular has recently shown potential as a new contrast agent with CEST [6,7], chemical exchange sensitive spin lock (CESL) [8–11] or chemical exchange based T_2 relaxation enhancement [12]. Dynamic CEST and CESL of glucose (glucoCEST/glucoCESL) have been performed to study tumor models in animals [6,13] and patients with glioblastoma [10,14] as it monitors the uptake and wash-out of glucose. Gluco-CEST spectra are obtained pre- and post-intravenous injection of exogenous glucose, and the difference between these spectra, so called glucose contrast enhancement (GCE) [6] or dynamic glucose enhanced (DGE) contrast [7,9,13,14] is assumed to mostly reflect the CEST effect of the glucose injection.

The DGE signal is relatively small, with values less than 5% in tumor areas at both 3 T and 7 T, and therefore vulnerable to subject's motion [10]. Even 1–2% of artifactual signal due to motion can hamper the sensitivity of intrinsic signal changes as it has been widely reported in other modalities including functional brain MRI (fMRI). For instance, blood oxygenation level dependent (BOLD) effects of interest are only a few percent in magnitude and therefore image time series fluctuation levels must be much lower than these small signal changes to accurately measure them. As motion correction and co-registration are mandatory steps in fMRI post-processing, similar attempts have been recently made in gluco-CEST/glucoCESL studies, which observed erroneous signal due to severe patient's movement [10,14]. Alternatively, use of immobilization devices was reported to reduce patient's motion [15], but this option may not be globally available due to a patient's discomfort level and may conflict with local ethics.

In the absence of motion constraints, it is essential to investigate the influence of motion in glucoCEST. To this end, we aimed to establish a systematic investigation of data post-processing in this study.

Abbreviations: CEST, chemical exchange saturation transfer; FLAIR, fluid attenuation inversion recovery; GRE, gradient-echo; MT, magnetization transfer; NOE, nuclear Overhauser effect.

* Corresponding author.
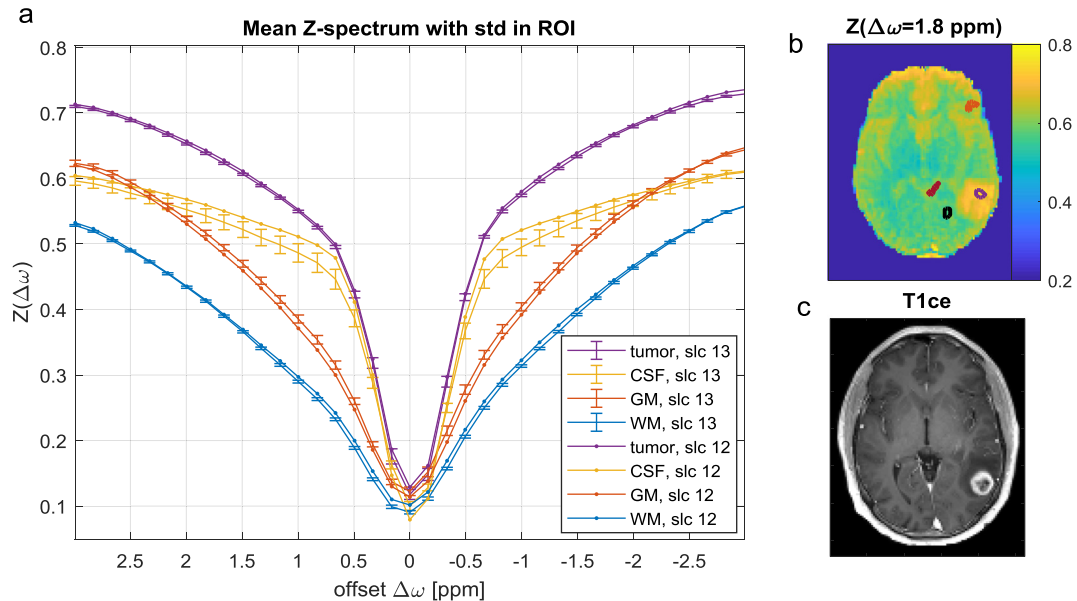*E-mail address:* moritz.zaiss@tuebingen.mpg.de (M. Zaiss).

Fig. 1. (a) B_0 corrected Z-spectra in different ROIs of two neighboring slices. (b) Z-value at 1.8 ppm used as the base 3D image in the following virtual dynamic scan. (c) T_1 contrast enhanced image of this slice depicting the tumor localization.

2. Methods

2.1. 3 T CEST MR imaging

3 T CEST imaging was performed on a whole body MRI system (PRISMA, Siemens Healthcare, Erlangen, Germany) on 1 healthy subject and one newly diagnosed brain tumor patient following an informed, written consent as approved by the local Ethics Committee of Tübingen and in agreement with all local regulations. A 3D snapshot-CEST acquisition [16] optimized for 3 T [17] consisted of a pre-saturation module of 5 s followed by a readout module of duration T_{RO} = 3.5 s, in which a train of RF and gradient spoiled gradient echoes with centric spiral reordering was acquired. Imaging parameters were FOV = 220 × 180 × 48 mm³, resolution 1.7 × 1.7 × 3 mm³, matrix size 128, 80% FOV in the first phase-encoding direction, phase encoding acceleration factor 2 and elliptical scanning; TE = 2 ms, TR = 5 ms, BW = 400 Hz/pixel, 18 slices, FA = 6° and elongation factor E = 0.5 (rectangular spiral reordered). The CEST saturation period consists of 1 Gaussian-shaped RF pulse, using a pulse duration of t_{pulse} = 100 ms, and mean B_1 = 3 μT, adapted from 9.4 T settings [18,19]. After the pulse, a crusher gradient was applied to spoil residual transversal magnetization. A separate WASABI measurement was acquired for B_0 and B_1 mapping [20].

In the patient, Z-spectrum data was obtained after saturation at 36 offsets in the range of ±3 ppm and normalized by M_0 scans with 12 s of relaxation and saturation at −300 ppm.

In the healthy subject, a scan was acquired with only 3 offsets, at 0.9, 1.2 and 1.5 ppm with 35 repetitions (20 min measurements total). The subject was instructed to lay still. From this dataset, only the dynamic motion from the SPM registration algorithm and the relative B_0 difference to the first image were used. The relative B_0 difference was calculated from the GRE phase images as described by Windschuh et al. [21].

2.2. Data evaluation

Z-spectrum data was corrected for motion using SPM [22], followed by B_0 inhomogeneity correction using the WASABI approach

[20]. CEST images were generated from the Z-value, $Z(\Delta\omega)$, given by the ratio of the saturated image $S_{sat}(\Delta\omega)$ and the fully relaxed image S_0

$$Z(\Delta\omega) = \frac{S_{sat}(\Delta\omega)}{S_0} \tag{1}$$

2.3. Motion and B_0 shift simulation

To simulate the effect of known translations and rotations, single-axis rigid body transformations employing linear interpolation were applied using custom written MATLAB code (The Mathworks, Natick, Massachusetts, USA) on a 3D stack acquired at a single frequency offset. Subsequently, the difference maps between pre-transformation and post-transformation were generated to simulate DGE contrast in the presence of motion according to the following relation

$$Z_{diff} = Z_{pre} - Z_{post}. \tag{2}$$

For B_0 shift simulation, small B_0 shifts were introduced in the Z_{post} data. The combined effect of motion and B_0 shifts was also investigated, with the B_0 shift introduced after the transformations were applied to all Z-spectrum data.

To study the effect of realistic motion, a motion pattern was obtained by SPM registration of dynamic subject data. The motion pattern and the concomitant inhomogenous B_0 alterations were applied as a series of rigid body transformations to the patient data stack to generate a dynamic measurement with controlled motion, and simulated DGE images were computed according to Eq. (2). The inverse motion transformation was then applied to simulate motion correction, and the dynamic contrast was recalculated for comparison.

3. Results & discussion

Fig. 1 shows Z-spectra in various tissue ROIs (grey matter, white matter, CSF and tumor) of B_0 corrected data, and from the same ROI evaluation but of a neighboring slice. Depending on different ROI positions as well as the frequency offset, the
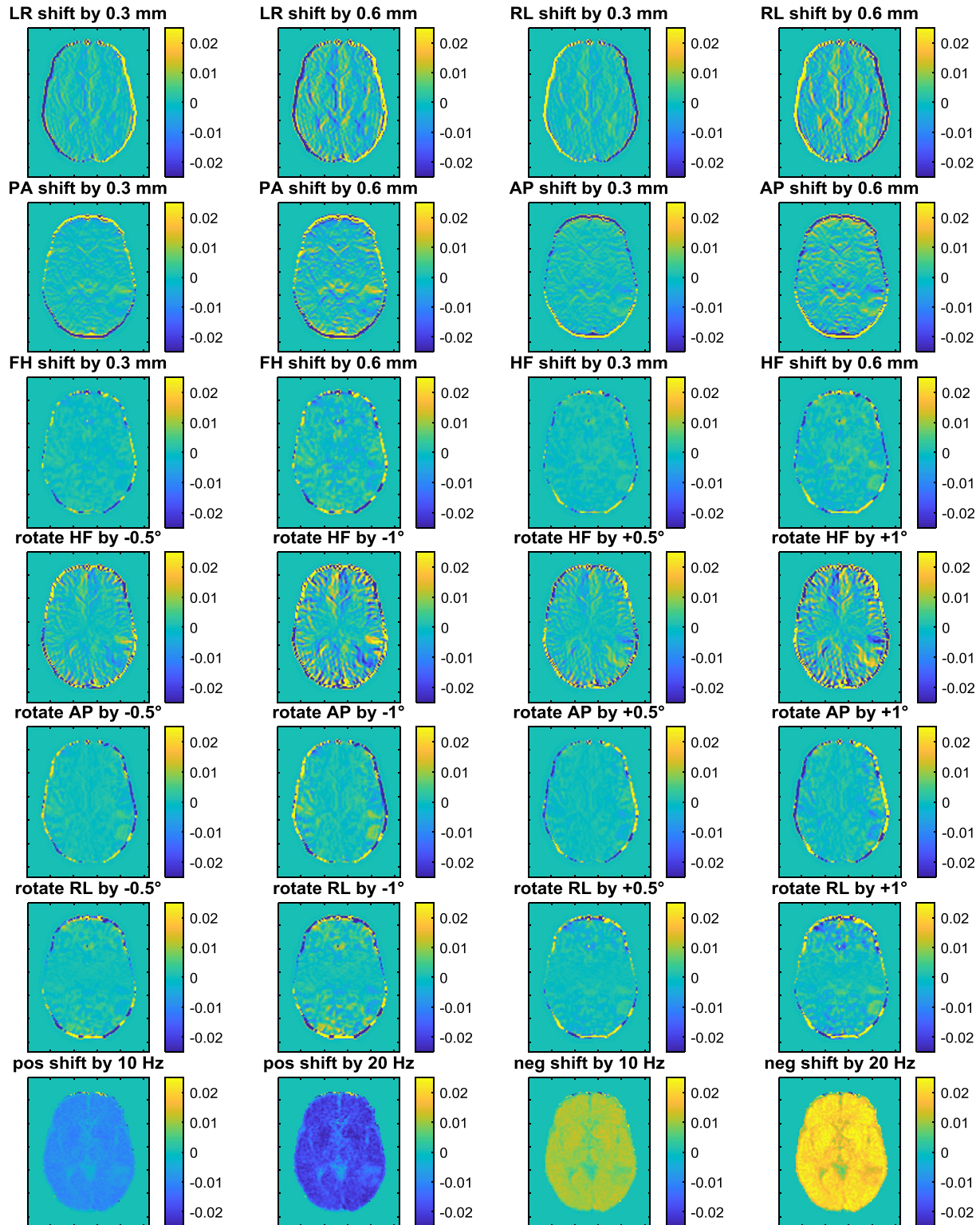
Fig. 2. Slice 11: Difference images after virtual rigid body translations (row 1–3), rotations (row 4–6) and B_0 shifts (bottom row) applied to the 3D baseline image as shown for one slice in Fig. 1. Abbreviations: RL left-right, AP anterior-posterior, HF head-foot.

variations in position or concomitant B_0 changes can lead to differences in the Z-spectra up to several percent. To simulate a relatively robust glucoCEST experiment, the 3D image given by the Z-value of the frequency offset 1.8 ppm is used, where the tissue difference as well the B_0 dependency is smaller than

at 1 ppm. Z (1.8 ppm) is shown in Fig. 1b and shows an endogenous CEST/MT contrast in the tumor area, as identified in the T_1-contrast enhanced image in Fig. 1c.

In Fig. 2 the virtual difference images Z_{diff} (Eq. (2)) after the rigid body transformations (applied on the CEST data of Fig. 1b) are

Table 1
Tumor ROI averaged values of all sub figures of Fig. 2 in same order of columns and rows. The tumor ROI was defined in the T1ce image (Fig. 1) by the ring enhancement.

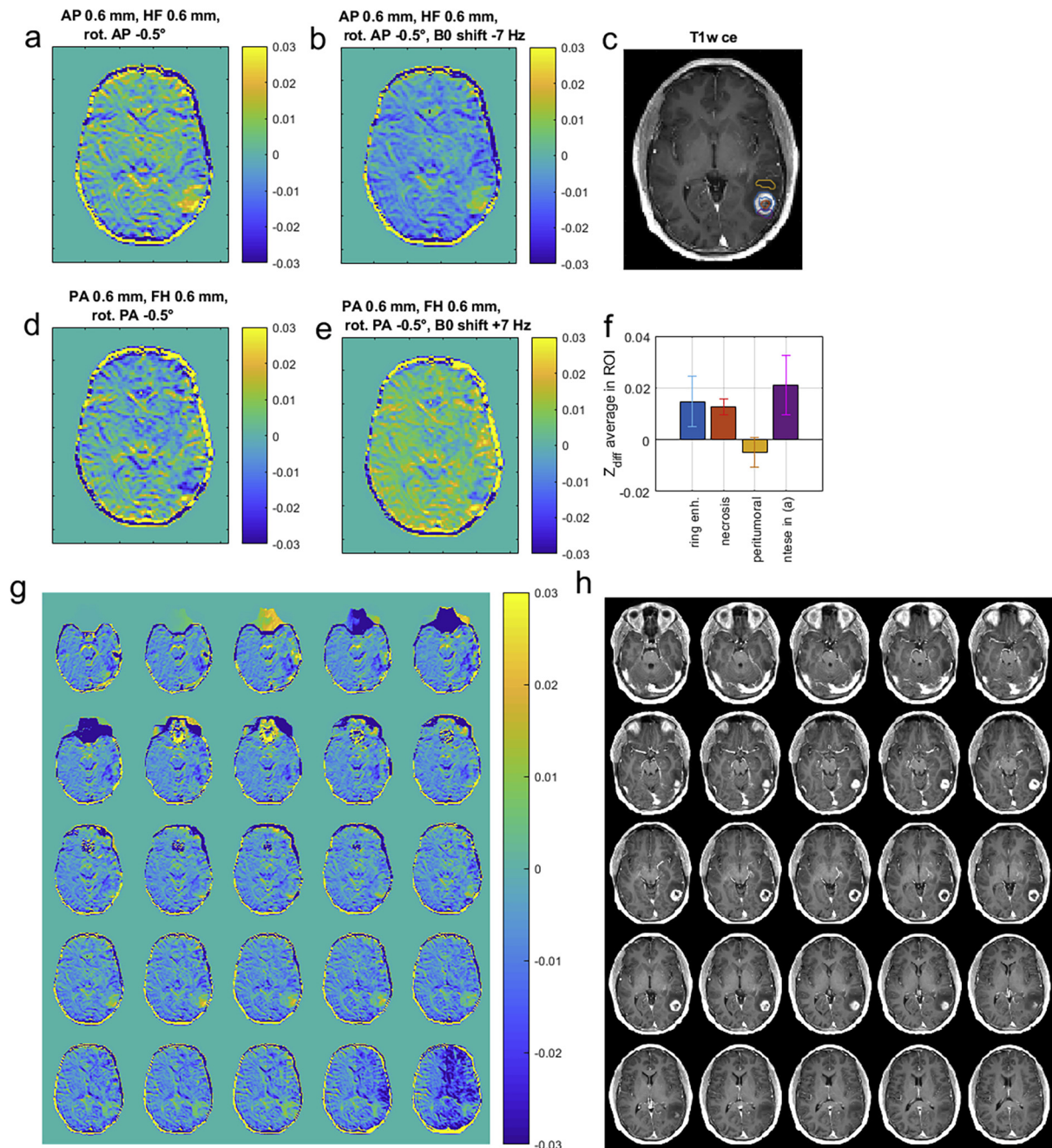| Z_{diff}	0.3 mm	0.6 mm	0.3 mm	0.6 mm
LR-RL	0.03%	0.07%	−0.01%	0.00%
PA-AP	−0.19%	−0.38%	0.20%	0.40%
FH-HF	−0.30%	−0.56%	0.33%	0.72%
rot HF	−0.27%	−0.56%	0.28%	0.59%
angle	−0.5°	−1°	0.5°	1°
rot. AP	0.52%	1.14%	−0.41%	−0.75%
rot. RL	−0.34%	−0.63%	0.41%	0.89%
	+10 Hz	**+20 Hz**	**−10 Hz**	**−20 Hz**
dB0	−1.65%	−3.29%	1.81%	3.63%

Fig. 3. Small motion worst case scenarios for difference images of a dynamic CEST contrast (a, b) showing signal in the tumor region similar to the gadolinium contrast-enhancement (c, g). The inverse transformations are depicted in (d, e) for completeness. (f) Shows ROI analysis of ROIs defined in (c) for the contrast in (a) exemplarily; up to 2% effect can be generated in worst case. (g) and (h) shows the same as (b) and (c), respectively, but for the whole 3D image with b and c included; in other slices than (b) hypointensities in the tumor region can be observed as well.
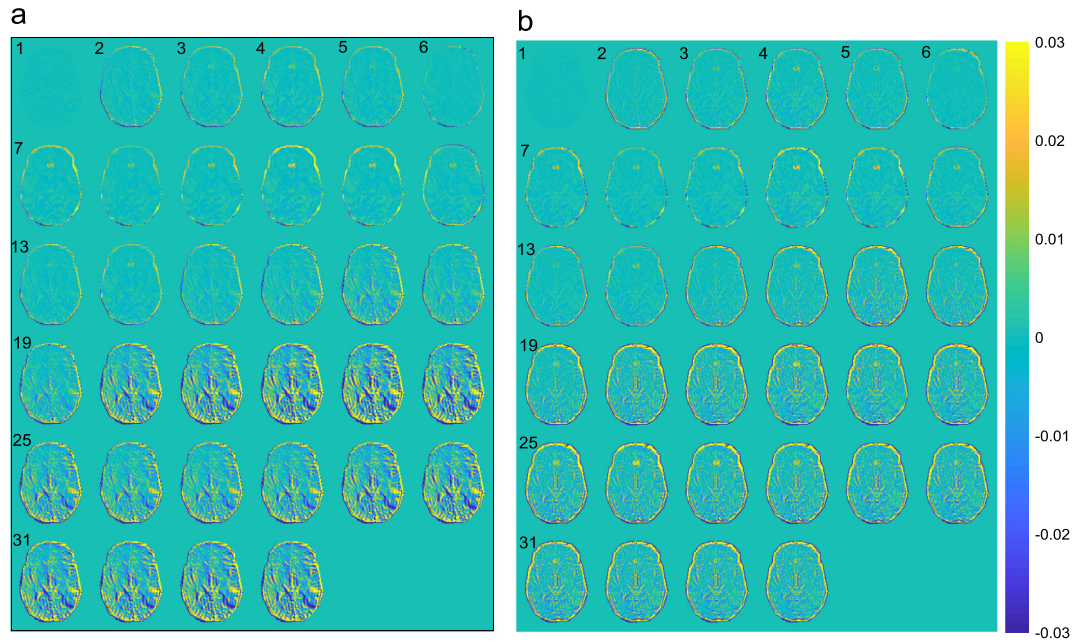
Fig. 4. Co-registration information of actual movement which occurred in a healthy subject scan (see Fig. 5a,b) and corresponding B_0 alterations were transferred to the virtual dynamic patient measurement for the full movement. The virtual dynamic contrast scan was created as difference to the original 3D volume (a). In the tumor area, artifacts can be seen in the range of 1% even with very small motion (scan 1–19 in a) and further increase to several percent for larger motion (scan 20–34 in a). After retrospective motion correction of this stack, visible in (b), residual artifacts are still observed, especially at tissue boundaries. For more detailed ROI evaluation see Fig. 5.

shown for translations only (rows 1–3), rotations only (rows 4–6) and B_0 shifts only (row 7). Typical motion artifacts visible as bright-dark patterns are observed in healthy tissue. Hyperintensities at ventricle edges are visible in the case of anterior-poster (AP) and right-left (RL) shifts, and signals in the sulci resembling vessels in the case of head-foot (HF) rotation. Certain motion (rotate RL, rotate AP, HF shift) can lead to untypical artifacts with hyperintensities only in the tumor area. Constant B_0 shift can be identified by strong signal changes in WM. Negative B_0 shifts can lead again to tumor hypointensities as compared to surrounding tissue. ROI averaged values of a tumor ROI for the same transformations can be found in Table 1.

In Fig. 3, a worst-case scenario for difference of images of Fig. 1b before and after transformations was created by applying combinations of different translations, rotations, (Fig. 3a) and B_0 shifts (Fig. 3b) to create a hyperintensity in the tumoral area (see Fig. 3c) and low signals everywhere else. This depicts the non-intuitive motion artifacts of dynamic CEST scans in tumoral areas, and that they can be easily mistaken as an uptake signal which nicely matches the necrotic or ring-enhancement region of the tumor. ROI analysis reveals that up to 2% pseudo CEST effect can be generated in such a worst case only by motion (Fig. 3f). The effect of the inverse transformation is shown in Fig. 3d and e for comparison. Fig. 3g shows the worst case of Fig. 3b again but for all slices of the 3D volume, together with all slices of the T_1-contrast enhanced images Fig. 3h. In this view, the same motion artifact (dark and bright pattern) below and above the tumor is visible. This further emphasizes that single slice evaluation is prone to non-intuitive and not identifiable motion artifacts.

In the last step, a measured dynamic movement transformation and the concomitant B_0 alterations were applied to the same tumor data to get an idea of a realistic motion artifact (Fig. 4). Similar patterns as illustrated in Fig. 2 are observed: for relatively small motion, pseudo-CEST effects in the range of 1% can be still observed. To test the effectiveness of an ideal motion correction,

the reverse transformation was applied to the same data (Fig. 4b). This did not result in a perfect image of zeros, but instead some residual artifacts are visible especially at tissue and tumor edges. This is mainly due to the interpolation during the transformation. We could of course perform the back-transformation without any interpolation, however this case is more realistic as in any motion correction of real data, an interpolation also has to be performed. This means that motion artifacts can in principal be suppressed to a great amount, but might still arise at tissue boundaries. In Fig. 5 the used motion data and ROI evaluations of the data in Fig. 4 are shown for the Z_{diff} contrast with and without motion correction, and with and without B_0 correction. This analysis reveals that motion is the dominant influence, yet, motion induced B_0 changes can still alter the effect strength by about 0.5% at 3 T, thus a combined motion and B_0 correction is expected to yield the best results. Going to higher field strengths than 3 T will make B_0 issues and their dynamic correction even more important.

In summary, the results indicate that motion correction is necessary even for small motions and its effectiveness must be verified to draw correct conclusions for any observed CEST effects below 2%. CEST effects below motion artifacts size are not reliable. Motion of DGE CEST imaging was already pointed out as a contributor to observed signal changes in the literature [10,14]. With the given analysis herein it is easier to identify certain changes as induced by motion, e.g. changes in grey matter can easily be due to rotations along the HF axis (see Fig. 2), and observed highlights at the edge of the ventricles might be an indicator for residual motion in RL or AP direction. As long as these pseudo CEST effects are present, interpretation of hyperintensities within regions of lesions have to be done carefully, and motion data should be compared with uptake curves. We recommend to carefully analyze the temporal signal-to-noise ratio (tSNR) employing repeated scans without glucose injection, as well as analysis of dynamic B_0 mapping, before moving to protocols with injection in healthy subjects and patients.
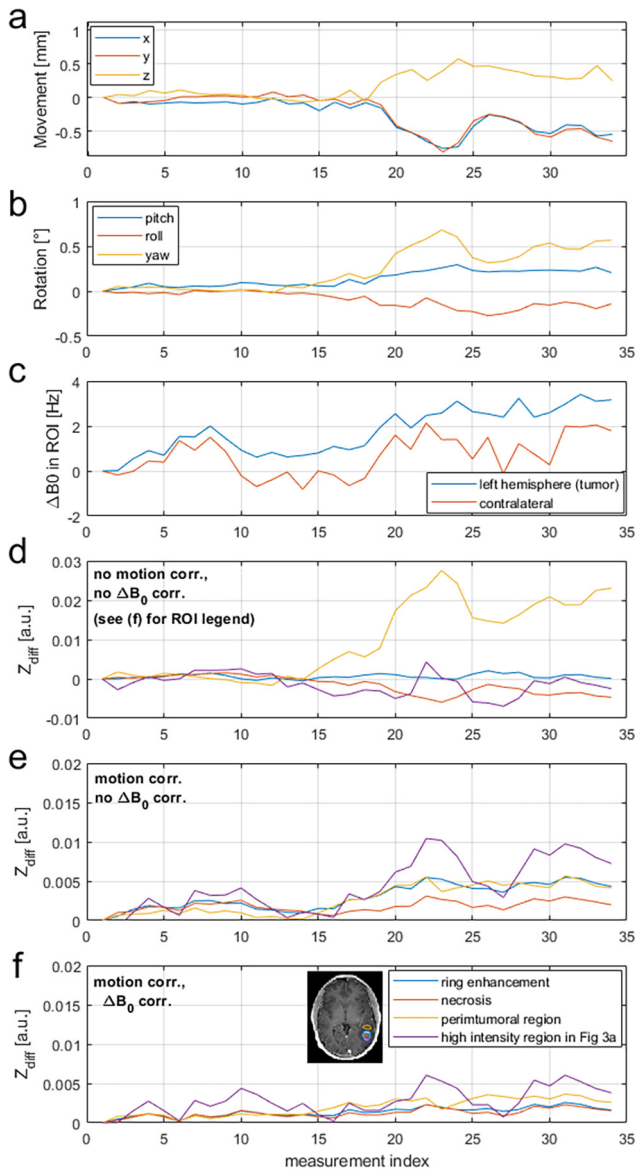
Fig. 5. Co-registration information of actual movement which occurred in a healthy subject scan (a, b) and corresponding B_0 changes (c). (d–f) ROI evaluations of data shown in Fig. 4 in ROIs as defined in T_1ce inlay in (d). (d) DGE contrast as a function of the measurement index without motion correction and without B_0 correction, (e) DGE contrast with motion correction but without B_0 correction, and (f) DGE contrast with both motion and B_0 correction. While motion is the dominant influence, motion induced B_0 changes can still alter the effect strength by about 0.5% (compare e, and f).

4. Conclusion

As dynamic CEST is extremely sensitive to motion artifacts, motion correction or mitigation is very important to not misinterpret false-positive signals as CEST agent uptake. Motion artifacts which can be identified in 3D acquisitions show some typical bright-dark patterns, but may show very non-intuitive hyperintensities depending on the slice and lesion geometry. When motion is effectively corrected, a more robust and sensitive dynamic CEST contrast will be achieved. However, even small residual motion artifacts can give rise to discernable signals which can resemble uptake of contrast agents. Attempting dynamic CEST measurements in patients without putting an effort into sophisticated motion correction is strongly ill-advised. Thus, we encourage MRI researchers to develop novel motion mitigation and correction approaches to improve robustness and reliability of dynamic and conventional CEST approaches at all field strengths.

References

[1] S.D. Wolff, R.S. Balaban, NMR imaging of labile proton exchange, J. Magn. Reson. 1990 (86) (1969) 164–169.
[2] S. Aime, D. Delli Castelli, E. Terreno, Novel PH-reporter MRI contrast agents, Angewandte Chemie 114 (2002) 4510–4512.
[3] N. Goffeney, J.W. Bulte, J. Duyn, L.H. Bryant, P.C. Van Zijl, Sensitive NMR detection of cationic-polymer-based gene delivery systems using saturation transfer via proton exchange, J. Am. Chem. Soc. 123 (2001) 8628–8629.
[4] K. Ward, A. Aletras, R. Balaban, A new class of contrast agents for MRI based on proton chemical exchange dependent saturation transfer (CEST), J. Magn. Reson. 143 (2000) 79–87.
[5] S. Zhang, M. Merritt, D.E. Woessner, R.E. Lenkinski, A.D. Sherry, PARACEST agents: modulating MRI contrast via water proton exchange, Acc. Chem. Res. 36 (2003) 783–790.
[6] S. Walker-Samuel, R. Ramasawmy, F. Torrealdea, M. Rega, V. Rajkumar, S.P. Johnson, S. Richardson, M. Goncalves, H.G. Parkes, E. Arstad, D.L. Thomas, R.B. Pedley, M.F. Lythgoe, X. Golay, In vivo imaging of glucose uptake and metabolism in tumors, Nat. Med. 19 (2013) 1067–1072.
[7] K.W.Y. Chan, M.T. McMahon, Y. Kato, G. Liu, J.W.M. Bulte, Z.M. Bhujwalla, D. Artemov, P.C.M. van Zijl, Natural D-glucose as a biodegradable MRI contrast agent for detecting cancer, Magn. Reson. Med. 68 (2012) 1764–1773.
[8] T. Jin, H. Mehrens, K.S. Hendrich, S.-G. Kim, Mapping brain glucose uptake with chemical exchange-sensitive spin-lock magnetic resonance imaging, J. Cereb. Blood Flow Metab. 34 (2014) 1402–1410.
[9] P. Schuenke, C. Koehler, A. Korzowski, J. Windschuh, P. Bachert, M.E. Ladd, S. Mundiyanapurath, D. Paech, S. Bickelhaupt, D. Bonekamp, H.-P. Schlemmer, A. Radbruch, M. Zaiss, Adiabatically prepared spin-lock approach for T1ρ-based dynamic glucose enhanced MRI at ultrahigh fields, Magn. Reson. Med. 78 (2017) 215–225.
[10] P. Schuenke, D. Paech, C. Koehler, J. Windschuh, P. Bachert, M.E. Ladd, H.-P. Schlemmer, A. Radbruch, M. Zaiss, Fast and quantitative T1ρ-weighted dynamic glucose enhanced MRI, Sci. Rep. 7 (2017) 42093.
[11] D. Paech, P. Schuenke, C. Koehler, J. Windschuh, S. Mundiyanapurath, S. Bickelhaupt, D. Bonekamp, P. Bäumer, P. Bachert, M.E. Ladd, M. Bendszus, W. Wick, A. Unterberg, H.-P. Schlemmer, M. Zaiss, A. Radbruch, T1ρ-weighted dynamic glucose-enhanced MR imaging in the human brain, Radiology 285 (2017) 914–922.
[12] N.N. Yadav, J. Xu, A. Bar-Shir, Q. Qin, K.W.Y. Chan, K. Grgac, W. Li, M.T. McMahon, P.C.M. van Zijl, Natural D-glucose as a biodegradable MRI relaxation agent, Magn. Reson. Med. 72 (2014) 823–828.
[13] X. Xu, K.W.Y. Chan, L. Knutsson, D. Artemov, J. Xu, G. Liu, Y. Kato, B. Lal, J. Laterra, M.T. McMahon, P.C.M. van Zijl, Dynamic Glucose Enhanced (DGE) MRI for combined imaging of blood-brain barrier break down and increased blood volume in brain cancer, Magn. Reson. Med. 74 (2015) 1556–1563.
[14] X. Xu, N.N. Yadav, L. Knutsson, J. Hua, R. Kalyani, E. Hall, J. Laterra, J. Blakeley, R. Strowd, M. Pomper, P. Barker, K. Chan, G. Liu, M.T. McMahon, R.D. Stevens, P.C. van Zijl, Dynamic Glucose-Enhanced (DGE) MRI: translation to human scanning and first results in glioma patients, Tomography 1 (2015) 105–114.
[15] J. Wang, J. Weygand, K.-P. Hwang, A.S.R. Mohamed, Y. Ding, C.D. Fuller, S.Y. Lai, S.J. Frank, J. Zhou, Magnetic resonance imaging of glucose uptake and metabolism in patients with head and neck cancer, Sci. Rep. 6 (2016) 30618.
[16] M. Zaiss, P. Ehses, Scheffler K. Snapshot-CEST, Optimizing spiral-centric-reordered gradient echo acquisition for fast and robust 3D CEST MRI at 9.4 T, NMR Biomed. 31 (2018) e3879.
[17] A. Deshmane, M. Zaiss, T. Lindig, K. Herz, M. Schuppert, C. Gandhi, Benjamin Bender, Ulrike Ernemann, Klaus Scheffler, 3D GRE snapshot CEST MRI with low power saturation for clinical studies at 3 T, Magn. Resonan. Med. 0 (2018), https://doi.org/10.1002/mrm.27569.
[18] K. Herz, C. Gandhi, M. Schuppert, A. Deshmane, K. Scheffler, M.C.E.S.T. Zaiss, Imaging at 9.4 T using adjusted adiabatic spin-lock pulses for on- and off-resonant T1ρ-dominated Z-spectrum acquisition, Magn. Reson. Med. (2018), https://doi.org/10.1002/mrm.27380.
[19] Gandhi Chirayu, Longo Dario, Anemone Annasofia, Herz Kai, Deshmane Anagha, Aime Silvio, Scheffler Klaus, in: Proceeding of 26th annual meeting of ISMRM 2018, Paris, o. J.,S.2233.

[20] P. Schuenke, J. Windschuh, V. Roeloffs, M.E. Ladd, P. Bachert, M. Zaiss, Simultaneous Mapping of Water Shift and B1 (WASABI)-application to field-inhomogeneity correction of CEST MRI data, Magn. Reson. Med. 77 (2017) 571–580.

[21] J. Windschuh, M. Zaiss, P. Ehses, J.-S. Lee, A. Jerschow, R.R. Regatte, Assessment of frequency drift on CEST MRI and dynamic correction: application to GagCEST at 7 T, Magn. Reson. Med. (2018), https://doi.org/10.1002/mrm.27367.

[22] SPM software - Statistical Parametric Mapping", can be found under https://www.fil.ion.ucl.ac.uk/spm/software/,o. J.